Twist-induced interlayer charge buildup in a WS_2 bilayer revealed by electron Compton scattering and density functional theory

A. Talmantaite,[1,2] Y. Xie,[2] A. Cohen,[3] P. K. Mohapatra,[3] A. Ismach,[3] T. Mizoguchi,[2] S. J. Clark,[1] and B. G. Mendis[1,*]

[1]*Department of Physics, Durham University, South Road, Durham, DH1 3LE, United Kingdom*

[2]*Institute of Industrial Science, University of Tokyo, 4-6-1, Meguro-ku, Tokyo, 153-8505, Japan*

[3]*Department of Materials Science and Engineering, Tel Aviv University, Tel Aviv 6997801, Israel*

(Received 16 May 2023; accepted 13 June 2023; published 27 June 2023)

Exotic properties emerge from the electronic structure of few-layer transition-metal dichalcogenides (TMDs), such as direct band gaps in monolayers and moiré excitons in twisted bilayers, which are exploited in modern optoelectronic devices and twistronics. Here, Compton scattering in a transmission electron microscope (TEM) is used to probe the nature of the interlayer electronic coupling in the TMD material WS_2. The high spatial resolution and strong scattering in the TEM enables a complete analysis of individual WS_2 domains, including their crystal structure. Compton measurements show that the electrons in an 18° twisted bilayer are more localized than in a monolayer. Density functional theory simulations reveal this is caused by a twist-induced charge buildup in the interlayer region, directly shielding the energetically unfavorable overlapping tungsten atoms. This unexpected result uncovers the precise role of twist angle on interlayer coupling, and therefore the physical properties that depend on it.

DOI: 10.1103/PhysRevB.107.235424

I. INTRODUCTION

Since the experimental realization of graphene by Novoselov *et al.* [1] and Geim and Novoselov [2], the field of 2D materials has grown rapidly to include other layered materials, such as elemental phosphorene [3] and silicene [4], the transition-metal dichalcogenides (TMD) [5] and group III/V chalcogenides [6], ceramic transition-metal carbides and nitrides (i.e., *MX*enes) [7], as well as polymers [8]. Novel properties related to the electronic structure emerge in the 2D limit, including ballistic transport of electrons [1], ferromagnetism [9], topological insulators [10], superconductivity [11], and indirect to direct band-gap transitions [12]. Further functionality is obtained by creating heterostructures of different 2D materials [13]. The weak van der Waals bonding between individual layers means that unlike their bulk counterparts, strain due to lattice mismatch is largely absent in 2D heterostructures, and hence there is no restriction in the choice of materials. In twistronics, the twist angle between individual layers creates moiré superlattices, which give rise to unexpected properties such as superconducting [14] and insulating [15] behavior in graphene, as well as moiré excitons in TMDs [16].

With such a wealth of new physics, and exploitation of 2D materials in next-generation transistors [17] and photonic devices [18], it is important to develop robust methods for electronic structure analysis of these materials. Angle-resolved photoemission spectroscopy (ARPES) [19–21] and scanning tunneling spectroscopy (STS) [22–24] are commonly used to measure the electronic structure of monolayers deposited on substrates. The sample must however be in a pristine condition with no surface hydrocarbons, so that thermal annealing in ultrahigh vacuum may be required prior to analysis, especially if chemical methods are used to exfoliate or transfer the sample onto new substrates [25]. The limited spatial resolution of ARPES also means that only large-area epitaxial monolayers grown by chemical vapor deposition (CVD) or molecular-beam epitaxy are suitable for analysis [19]. Smaller flakes can be analyzed in a synchrotron using nano-ARPES at submicrometer resolution, but no information is available on the structure of the analyzed region, which is important for twisted bilayers. STS can achieve atomic resolution, although care must be taken with potential artifacts due to tip-sample separation and tip-induced band bending [23,24]. A more versatile electronic structure analysis method that is applicable to a wide range of 2D materials, is easy to interpret, and provides complementary structural information, such as number of layers, twist angle etc., is therefore required.

In a transmission electron microscope (TEM) the electronic structure can be analyzed via Compton scattering of the high-energy primary electron with individual electrons in the solid [Fig. 1(a)] [26,27]. In the impulse approximation [26], the primary electron imparts some of its energy and momentum to a solid-state electron in a two-body collision that is independent of other solid-state electrons and atomic nuclei. For a sample that is illuminated by a tilted parallel electron beam [Fig. 1(b)] the Compton inelastic signal appears as a broad peak at large scattering angles φ in an electron energy-loss spectrum [EELS; Fig. 1(c)]. The broadening of

*Corresponding author: b.g.mendis@durham.ac.uk

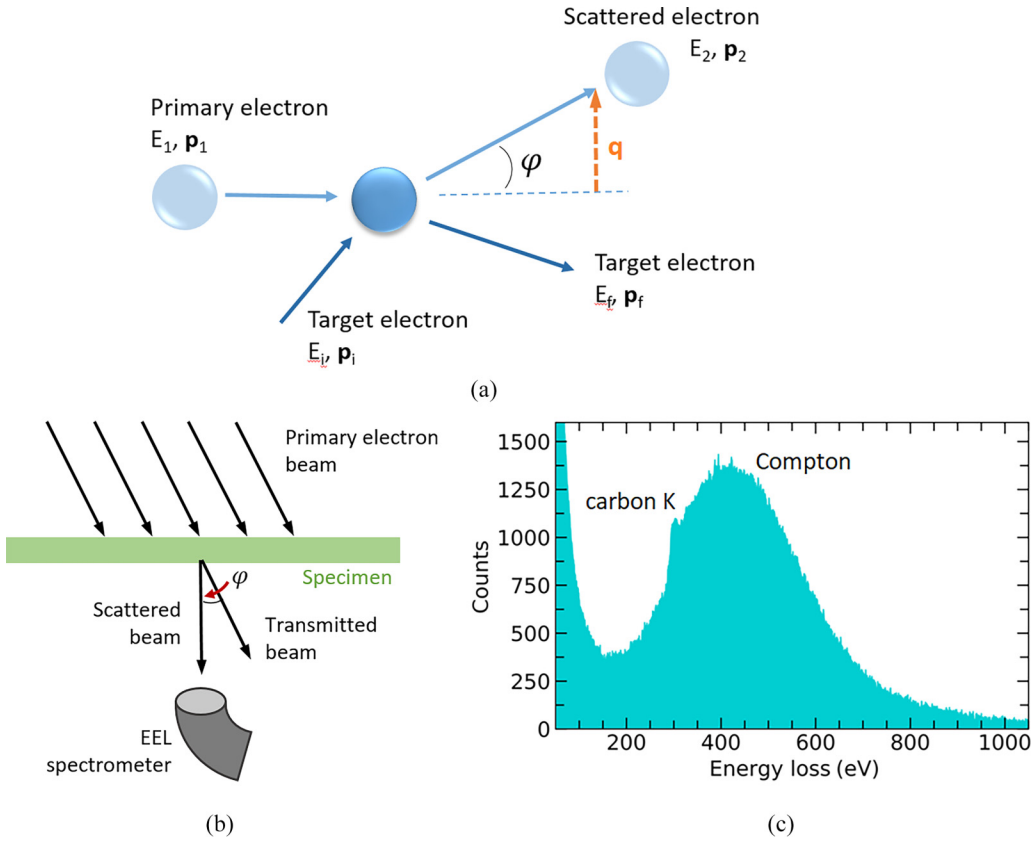

FIG. 1. (a) Compton scattering event between the primary high-energy electron and target electrons in the solid. (E_1, $\mathbf{p}_1$) and (E_2, $\mathbf{p}_2$) are the energy and momentum of the primary electron before and after Compton scattering, respectively, while (E_i, $\mathbf{p}_i$) and (E_f, $\mathbf{p}_f$) are the corresponding values for the target electrons. φ is the Compton scattering angle, and $\mathbf{q}$ is the scattering vector. (b) Experimental EELS setup for Compton scattering measurements in the TEM. An off-axis EELS spectrum for monolayer WS_2 with Compton profile is shown in (c). Also note the presence of the carbon *K* edge due to hydrocarbon contamination on the sample.

the Compton peak is due to the momentum distribution of the solid-state electrons (Doppler broadening effect). The Compton profile is therefore directly related to $J(p_z)$, the projected density of electrons with momentum component p_z along the scattering vector direction [28], a quantity that can be derived from the electronic band structure of the material. Two-dimensional materials are ideal for Compton analysis in the TEM for several reasons. First, the strong interaction of the primary electron beam with the specimen means that a Compton signal can be obtained from a monolayer within only a few minutes. Secondly, the illumination area of the parallel beam on the sample is only a few hundred nanometers in diameter (∼600 nm in this study, although smaller diameters are possible on our TEM), which is similar to nano-ARPES, but with the additional advantage that the structure and chemistry of the analysis region are readily obtained through complementary TEM techniques.

Here, we present electron Compton scattering results from single flakes of monolayer and 18° twisted bilayer WS_2. The material shows an indirect to direct band-gap transition in the monolayer limit [29,30]. Experimental $J(p_z)$ data combined with density functional theory (DFT) simulations reveal an unexpected localization of electronic charge in the interlayer region of the bilayer. The charge buildup is structurally induced, with higher charge concentrations found between "wrong bonds" of overlapping tungsten atoms. The twist angle has been shown to alter the optical, vibrational, and electrical properties of bilayer TMDs [31]. By combining TEM with DFT we are able to uncover the precise nature of the interlayer coupling in twisted bilayers. The results are significant for twistronic applications, where the twist angle is used to modify the material physical properties.

II. METHODS

A. WS_2 sample fabrication

WS_2 films were grown on a sapphire substrate via growth-etch metal organic chemical vapor deposition (GE- MOCVD) at a temperature of 850 °C and 50-Torr pressure. The method involves a pulsed delivery of tungsten carbonyl ($W(CO)_6$) and di-*tert*-butyl sulfide precursors with a supply of H_2O vapor between the growth cycles. Here, H_2O vapor acts as an etchant for part of WS_2 nuclei and carbon contaminants ensuring the growth of large WS_2 domains. For more details, see Refs. [32,33]. After growth, the WS_2 films were transferred onto a holey carbon TEM grid using the surface-energy assisted process [34]. Specifically, a layer of polystyrene was spin coated on the substrate and baked to secure good adhesion between WS_2 and polymer. The assembly was then immersed in deionized water, causing delamination of the WS_2/polystyrene film from the substrate due to hydrophobic and hydrophilic properties of WS_2 and sapphire,

respectively. The film was then transferred onto the TEM grid and the remaining polystyrene coating dissolved in toluene.

B. Transmission electron microscopy

TEM was performed on a JEOL 2100F field-emission gun microscope operating at 200 kV. A Gatan Rio camera was used for recording the high-resolution electron microscopy (HREM) images and selected-area electron diffraction (SAED) patterns. The parallel electron beam was tilted for Compton measurements using the beam shift/tilt coils in centered dark-field imaging mode. EELS spectra were recorded in imaging mode on a Gatan Tridiem spectrometer at 0.5 eV per channel dispersion. The EELS collection semiangle of 5.3 mrad is determined by the 20-μm objective aperture used for centered dark-field imaging. The Compton scattering angle was 39.5 mrad, and the scattering vector was along $10\bar{1}0$ for monolayer WS_2 and bisecting the $10\bar{1}0$ Bragg reflection pairs for twisted bilayers. A holey carbon TEM grid was used for Compton measurements on amorphous carbon, with a slightly larger scattering angle of 41.2 mrad. A power-law model was used to subtract the background under the Compton peak, which was then converted to a $J(p_z)$ profile, assuming the impulse approximation and the equations given in Ref. [35]. Only the high energy-loss side of the Compton profile was used for analysis in order to avoid the overlap with the carbon K edge [see Fig. 1(c)].

C. Density functional theory

DFT simulations were performed using the CASTEP electronic structure code, which is a plane-wave pseudopotential method to solve a set of single-electron Kohn-Sham equations [36]. For WS_2, electron-ion interactions were described using an ultrasoft pseudopotential formalism, while the meta-generalized gradient approximation (meta-GGA), regularized SCAN functional [37] was used to approximate electron exchange and correlation. The plane-wave basis-set cutoff (350 eV) and k-point sampling ($3 \times 3 \times 1$) for Brillouin-zone integrations was converged to better than 5 meV per atom. Geometry optimizations were considered to be converged when the forces between atoms were below 0.05 eV/Å. The c axis of the supercell was expanded to 38.37 Å to include a vacuum region, which minimized artifacts caused by periodic boundary conditions. The electron group velocity and density of states in k space were calculated from the gradient of the electronic band structure [38], from which p_z and $J(p_z)$ can be derived. Electronic bands up to 15 eV below the highest occupied level were used for calculating $J(p_z)$. While this does not give $J(p_z)$ for all electrons in the solid, it is sufficient to accurately calculate the difference $\Delta J(p_z)$ between monolayer and bilayer, since the major changes due to interlayer coupling involve electronic states within only 1 eV of the valence-band maximum [39]. Further integration of electronic states to lower energies resulted in a "spike" around $p_z = 0$, since the band structure of these semicore states was largely flat. To avoid artifacts due to the spike, $J(p_z)$ at small values of p_z ($\leqslant 0.18$ a.u.) were discarded. Furthermore, the finite sampling of the band structure produced some "noise" in the $J(p_z)$ data (see Supplemental Material [40]), which was smoothed using a Savitzky-Golay filter [41].

III. RESULTS AND DISCUSSION

A. Structural characterization and Compton scattering

Only freestanding regions of WS_2 suspended over vacuum in the holey carbon TEM grid were used for Compton analysis. The sample consisted of single monolayers as well as bilayers, the latter created by monolayer folding during TEM preparation. Representative HREM lattice images and SAED patterns for monolayer and bilayer WS_2 are shown in Fig. 2. The monolayer does not contain any noticeable defects, such as vacancies or grain boundaries, although there is some hydrocarbon contamination on the surface [Fig. 2(a)], as is typical for 2D materials. The HREM image for the bilayer shows a distinct moiré pattern [Fig. 2(d)] due to a 17° twist angle between the individual layers, as evidenced by pairing of the Bragg reflections in the SAED pattern [Fig. 2(f)]. The twist angle was not constant, but varied between different bilayers.

An off-axis EELS spectrum at large momentum transfer has a significantly weaker intensity compared to a standard on-axis EELS spectrum that is acquired close to zero momentum transfer. Electron beam damage of the specimen, especially sputter damage of chalcogen atoms in TMDs, during the relatively long acquisition times required for Compton analysis could therefore be an issue. DFT calculations have shown that sulfur vacancies in monolayer MoS_2 reduce the band gap by forming defect states, although the vacancy concentration where noticeable changes are observed is extremely large, i.e., one or more sulfur vacancies in every 3×3 MoS_2 unit cell [39]. The evolution of damage in monolayer WS_2 by a 200-kV electron beam was investigated by acquiring a time series of HREM images at different stages of electron-beam exposure (Fig. 3). Atomic-size, isolated vacancies are observed after 30 s, which coalesce into larger clusters ($\leqslant$ 1 nm) after approximately 100 s. Electron-beam damage was also examined by monitoring the intensity of a higher-order $3\bar{3}00$ Bragg reflection as a function of time (see Supplemental Material [40]). The Bragg intensity only started decreasing after ~120 s, indicating that the long-range order of WS_2 is still largely preserved until that time, despite the appearance of vacancies. The maximum acquisition time for an electron Compton measurement, using the same experimental conditions as HREM and SAED, was therefore limited to 60 s to avoid any artifacts due to beam damage.

The band gap in multilayer WS_2 is indirect, with the valence-band maximum at the Γ point and conduction-band minimum at the Q point along the Γ-K reciprocal direction [42]. The electronic states at these extrema contain contributions from the out-of-plane chalcogen p orbitals, and are therefore sensitive to interlayer coupling. Reducing the number of layers to at most only a few layers results in a decrease (increase) in the valence- (conduction-) band energy at the Γ (Q-) point. For a monolayer the smallest energy gap is therefore a direct band gap at the K point [42]. The K-point electronic states comprise a mixture of transition metal d electrons and chalcogen p-orbital electrons, and are largely unaffected by interlayer coupling. In fact, the largest changes to the electronic structure with number of layers occur close to the Γ point along the Γ-K direction. The electron Compton signal is therefore acquired with the scattering

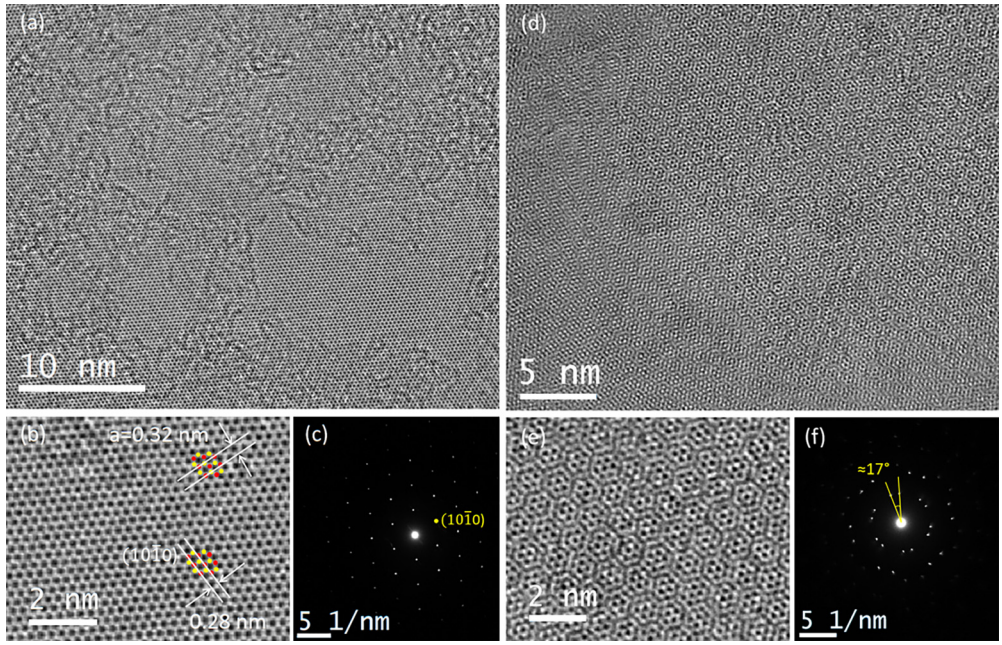

FIG. 2. HREM images of monolayer WS_2 under different magnifications in (a) and (b), and (c) corresponding SAED pattern. Red and yellow dots in (b) are a guide to the eye for approximate tungsten and sulfur atom positions, respectively. Some surface hydrocarbon contamination is evident in (a). HREM images of a 17° twisted bilayer under different magnifications are shown in (d) and (e), while (f) is the corresponding SAED pattern.

vector along the $10\bar{1}0$ reciprocal direction. For bilayers the scattering vector was chosen to bisect a pair of $10\bar{1}0$ reflections; the projected momentum component p_z of electrons in a Compton $J(p_z)$ measurement would then deviate from the true Γ-K direction by half the twist angle.

The Compton scattering angle φ is another important experimental parameter. In measurements at small values of φ, which have short acquisition times due to the smaller momentum transfer, the Compton peak appears at lower energy losses in the EELS spectrum. Hence, fewer electrons can participate in Compton scattering, since the electron binding energy must be smaller than the Compton energy loss. Furthermore, the Compton profile will be more prone to background subtraction artifacts from the tail of the plasmon peak [26]. The scattering angle in our study was set to 39.5 mrad, which placed the Compton peak maximum at ∼420 eV [Fig. 1(c)], higher than the carbon K-edge artifact at 284 eV due to surface hydrocarbon contamination [Fig. 2(a)]. At these conditions, all sulfur electrons apart from the core K-shell electrons undergo Compton scattering, while for the heavier tungsten atoms only the outer P, O-shell and $4d$, $4f$ electrons are Compton scattered [43] (see Supplemental Material [40]). This is, however, sufficient to probe the electronic structure due to interlayer coupling in WS_2. Recent work has also indicated that reliable $J(p_z)$ data can be obtained for "soft" Compton collisions at small scattering angles, where only the valence electrons are excited [35].

Figure 4(a) shows $J(p_z)$ profiles measured along $10\bar{1}0$ for three different WS_2 monolayers. The area under the curve is proportional to the number of electrons undergoing Compton scattering [28], but here the area has been normalized to unity, since we expect some (unknown) contribution from the surface hydrocarbon contamination. There is a high degree of reproducibility between the measurements, despite potential contamination artifacts. For example, the difference $\Delta J(p_z)$ between any two of the monolayers [e.g., Fig. 4(b)] showed only random variations, with a magnitude of no more than 0.06 normalized units [see also Supplemental Material [40] for further $\Delta J(p_z)$ difference spectra between monolayers]. Bragg diffraction in a crystal is known to introduce artifacts in electron Compton measurements, due to the Bragg beams being secondary sources of Compton scattering [44]. However, diffraction artifacts are minimal for a WS_2 monolayer, where the unscattered beam intensity is measured to be at least two orders of magnitude larger than the Bragg beams. Hence, asymmetric EELS Compton profile shapes, which are characteristic of Bragg diffraction [44], are not observed. In Fig. 4(c), the normalized $J(p_z)$ curves for two bilayers with twist angles of 18° and 12° are superimposed, and the corresponding $\Delta J(p_z)$ difference profile is plotted in Fig. 4(d) (see Supplemental Material for bilayer SAED patterns and Compton scattering vectors [40]). $\Delta J(p_z)$ shows a more systematic variation, with the largest differences occurring around $p_z = 0$. This could indicate the importance of the twist angle on the bilayer electronic structure, although experimental artifacts due to varying amounts of hydrocarbon contamination and/or error in the choice of scattering vector cannot be ruled out (for the 12° twisted bilayer the scattering vector passed through a Bragg beam, rather than bisecting the pair of Bragg spots).

B. Electronic structure changes due to interlayer coupling

Figure 5(a) shows a comparison of the normalized $J(p_z)$ for a monolayer and the 18° twist-angle bilayer. The monolayer $J(p_z)$ is taller and narrower compared to the bilayer. To quantify the changes, the $\Delta J(p_z)$

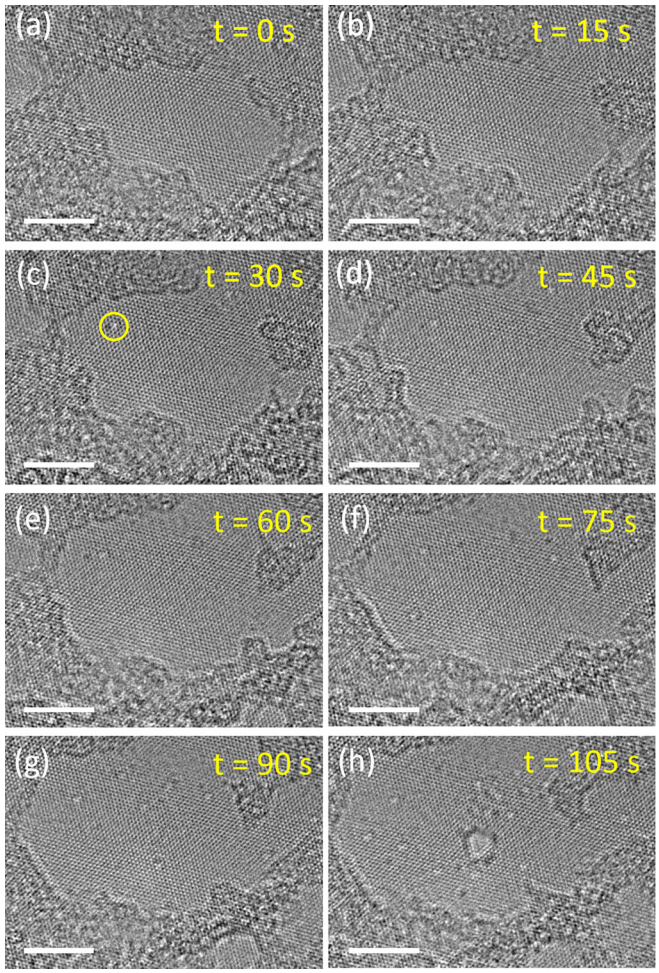

FIG. 3. Defect formation in monolayer WS_2 as a function of electron-beam irradiation time (seconds). Circled region in (c) is an observable vacancy cluster due to electron-beam damage. Also note the presence of hydrocarbon contamination on the sample. Scale bar represents 5 nm.

$= [J(p_z)_{\text{monolayer}} - J(p_z)_{\text{bilayer}}]$ difference profile was divided by the $J(p_z)$ value for the monolayer at $p_z = 0$ (this method of plotting enables a direct comparison with DFT simulation; see Methods, Sec. II). The resulting fractional difference profile [Fig. 5(b)] has largest values for electron momentum components p_z close to zero. This is consistent with previous DFT results, which showed that interlayer coupling had the strongest effect on the valence-band maximum around the Γ point, while the K point remained virtually unchanged [12,42]. The monolayer has a higher electron density for p_z values between zero and ≈1.4 atomic units (a.u.), meaning the electrons are more localized along the Γ-K direction in the bilayer. The experimental data were also compared with DFT simulations using CASTEP [36]. Normalized $J(p_z)$ profiles simulated from unit cells of WS_2 monolayer and bilayer with 60° (perfect "*AB*" stacking) and 18° twist angle are shown in Fig. 5(c). The coincident site lattice for the 18° WS_2 bilayer was computer generated [44] and lattice relaxed using DFT. The algorithm in Ref. [45] optimizes the multiplicity of each constituent lattice, such that the deformation required to generate a coincident site lattice is as small as possible; see Supplemental Material [40] for more details about the supercell. Note that the simulated $J(p_z)$ profiles have been smoothed to reduce noise from finite sampling of the electronic band structure. The raw data can be found in the Supplemental Material [40], and the simulation procedure is described in Methods, Sec. II. The twist angle has an important effect on the bilayer electronic structure. At 18° twist angle the electrons are considerably more localized than in a perfectly stacked bilayer, as is evident from a much broader $J(p_z)$ profile for the former [Fig. 5(c)].

Previous investigations on bilayer graphene [46] and TMD bilayer heterostructures (e.g., MoS_2-WS_2) [47], have shown significant atomic relaxation at small twist angles (< 1°). The geometric moiré pattern contains local regions of ideal *AB* stacking, as well as higher-energy "*AA*" stacking. Upon relaxation, the material rearranges to form larger *AB* domains. However, as the twist angle increases beyond 1°, the local atomic configuration changes more rapidly, and domain formation is not observed [46,47]. This is also true for the bilayers in this study, where the twist angle is > 10°. HREM [Fig. 2(e)] shows a geometric moiré pattern rather than domains, and the SAED pattern [Fig. 2(f)] does not reveal any satellite reflections arising from an underlying domain structure [46]. The DFT relaxed supercell for the 18° bilayer also did not show any evidence for domains (see Supplemental Material [40]). Finally, if domains were to form, the $J(p_z)$ for the twisted bilayer should agree more closely with perfect stacking. All of these observations indicate that domain formation cannot explain the changes in $J(p_z)$ with twist angle.

To determine the origin of localized electron behavior, isosurfaces of the electron density are plotted for the 18° twisted bilayer. Figure 6(a) shows the isosurface for an electron density $0.000\,35\rho_{\text{max}}$, where ρ_{max} is the maximum electron density. Charge buildup in the interlayer region is observed, which is not present in the *AB* stacked bilayer (see Supplemental Material [40]). The amount of interlayer charge is estimated to be 0.13% or ∼9 electrons per supercell. A precise calculation is difficult, since there is some overlap with the electron density assigned to atoms in the top and bottom WS_2 layers, specifically low-energy, outer electron orbitals that have a large spatial extent. Note that only the outermost valence electrons are used to calculate the $J(p_z)$ profiles in Fig. 5(c) (see Methods, Sec. II), and therefore the changes in the profile shape with twist angle are more pronounced than what would be expected if all the electrons were included. The interlayer charge buildup is strongest in regions where tungsten atoms from the two WS_2 sheets are close to vertical alignment [Fig. 6(b)]. To quantify this further, we calculated the pair separation between two W atoms in the top and bottom layer which are "nearest neighbors" when viewed in projection along the c axis of the bilayer. Figure 6(c) shows the correlation between the nearest-neighbor pair separation projected in the *ab* plane and along the c axis. For ideal *AB* stacking the *ab*-plane pair separation is 1.8 Å, but due to the 18° twist angle the spacings here are much smaller, and there is also an example of two W atoms in perfect vertical registry [Fig. 6(b)]. As a general trend, the pair separation along the c axis increases as the nearest-neighbor W atoms approach vertical alignment. The c-axis pair separations for the twisted bilayer are much larger than the ideal value of 6.2 Å for *AB* stacking. Vertically aligned W atoms are energetically

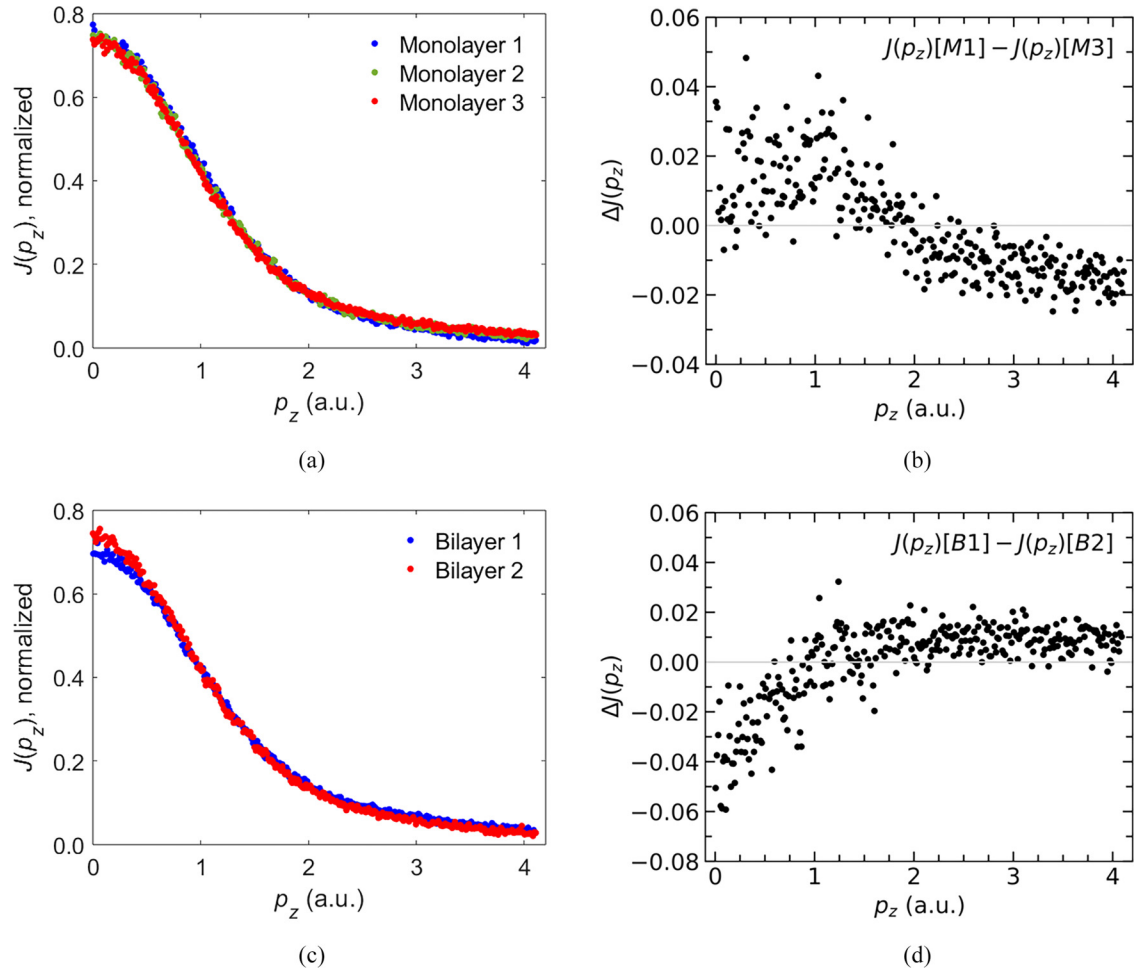

FIG. 4. (a) Experimental $J(p_z)$ profiles for three different WS_2 monolayer flakes. Area under the curve is normalized to unity. Data points for "monolayer 2" are partly hidden by strong overlap between profiles. $\Delta J(p_z)$ difference profile for monolayers 1 and 3 is shown in (b). (c) Normalized, experimental $J(p_z)$ profiles for two WS_2 bilayer flakes with twist angle 18° (bilayer 1) and 12° (bilayer 2). Corresponding $\Delta J(p_z)$ difference profile is shown in (d).

unfavorable; the results indicate that the energy is reduced by a local increase in the layer separation, accompanied by charge buildup in the interlayer region. Interlayer charge has also been reported in Bi_2Se_3-TMD heterostructure bilayers [48] using DFT. That study also claimed indirect experimental evidence for the interlayer charge using SAED, although dynamical electron diffraction from the moiré superlattice cannot be ruled out. The twist angle in MoS_2 bilayers has been shown to alter the band gap, Raman vibrational modes, and electron mobility [31,49]. Nano-ARPES measurements reveal the largest changes in the electronic structure to be around the valence-band maximum at the Γ point [50], while DFT simulations indicate that the changes are driven by the interlayer spacing for the different twist configurations [31,49]. There was no investigation into interlayer charge buildup, although based on the current evidence for WS_2, it is speculated that this should also occur in MoS_2 bilayers.

The fractional difference profiles, i.e., $\Delta J(p_z)$ divided by the monolayer $J(p_z)$ value at the origin, for CASTEP simulated monolayer and bilayer structures are shown in Fig. 5(d). The introduction of the 18° twist angle gives better agreement with the experimental result compared to perfect *AB* stacking [Fig. 5(b)], although important differences still remain. For example, the simulation shows a small peak between $p_z = 0.8$ and 1.2 a.u., due to higher $J(p_z)$ values for the monolayer in this momentum range [Fig. 5(c)], which can be attributed to electronic states within 1 eV from the valence-band maximum. The small peak is, however, not observed in the experiment, although this could partly be due to the large scatter in data points at the corresponding p_z values. A further discrepancy is that the simulated fractional $\Delta J(p_z)$ value at $p_z = 0$ is larger by a factor of ∼5 compared to experiment.

A potential source of artifacts is the hydrocarbon contamination present on the WS_2 surface [Fig. 2(a)]. The $\Delta J(p_z)$ difference spectrum will largely remove the Compton signal from the hydrocarbons, although a residual contribution could still be present if monolayer and bilayer have different amounts of contamination. To estimate its effect, a normalized $J(p_z)$ profile for amorphous carbon was measured using a holey carbon TEM specimen [Fig. 5(e)]. The profile was then smoothed and a small fraction either added or subtracted from the simulated, fractional $\Delta J(p_z)$ difference plot between WS_2 monolayer and 18° twist bilayer. Figure 5(f) shows representative graphs for residual carbon values between 10% undersubtracted to 10% oversubtracted. Undersubtraction corresponds to higher contamination in the monolayer

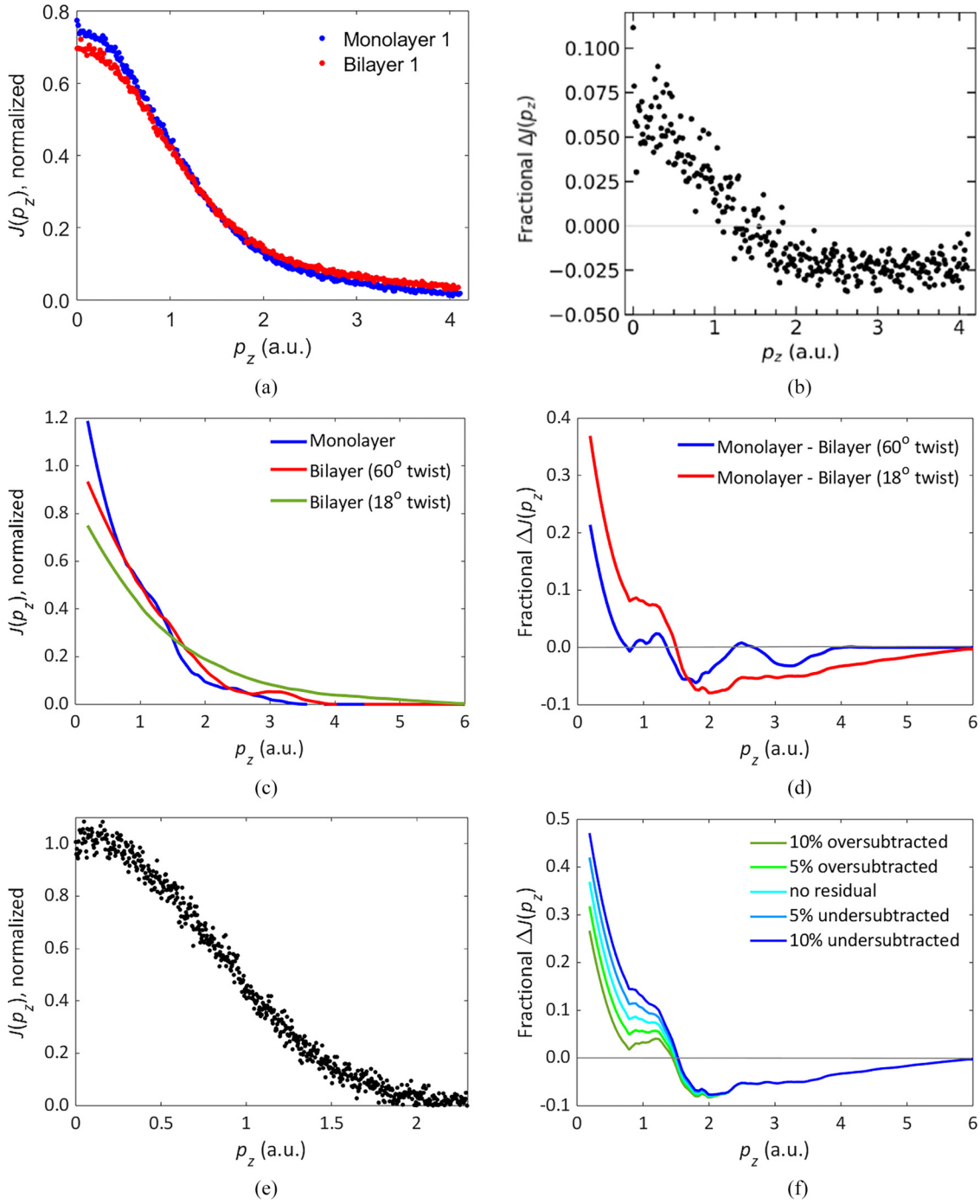

FIG. 5. (a) Normalized, experimental $J(p_z)$ profiles for monolayer and 18° twist bilayer WS_2; (b) the $\Delta J(p_z) = [J(p_z)_{\text{monolayer}} - J(p_z)_{\text{bilayer}}]$ difference profile expressed as a fraction of the monolayer $J(p_z)$ value at $p_z = 0$. (c) Normalized, DFT simulated $J(p_z)$ profiles for WS_2 monolayer, and bilayer with 60° and 18° twist angles. (d) Corresponding $\Delta J(p_z)$ difference profiles between monolayer and bilayer expressed as a fraction of the monolayer $J(p_z)$ value at $p_z = 0$. (e) Experimental $J(p_z)$ profile for amorphous carbon. Area under the curve has been normalized to unity. In (f) varying amounts of residual carbon $J(p_z)$ are added or subtracted from the fractional $\Delta J(p_z)$ curve in (d) between monolayer and 18° twist bilayer.

compared to bilayer, and vice versa for oversubtraction. A range of ±10% carbon was considered to be realistic levels for residual contamination. The bilayers are formed by monolayer folding during TEM specimen preparation, which should result in a smaller fraction of surface contamination compared to a monolayer, since the folded interiors are less exposed to the outside environment. In this scenario, the carbon signal is undersubtracted, which leads to higher fractional $\Delta J(p_z)$ values close to the origin [Fig. 5(f)]. A residual Compton signal from hydrocarbon contamination is therefore unlikely to be the dominant cause of the discrepancy between simulation and experiment, though it will have some contribution. However, the presence of contamination in the interlayer region is likely to reduce coupling between the

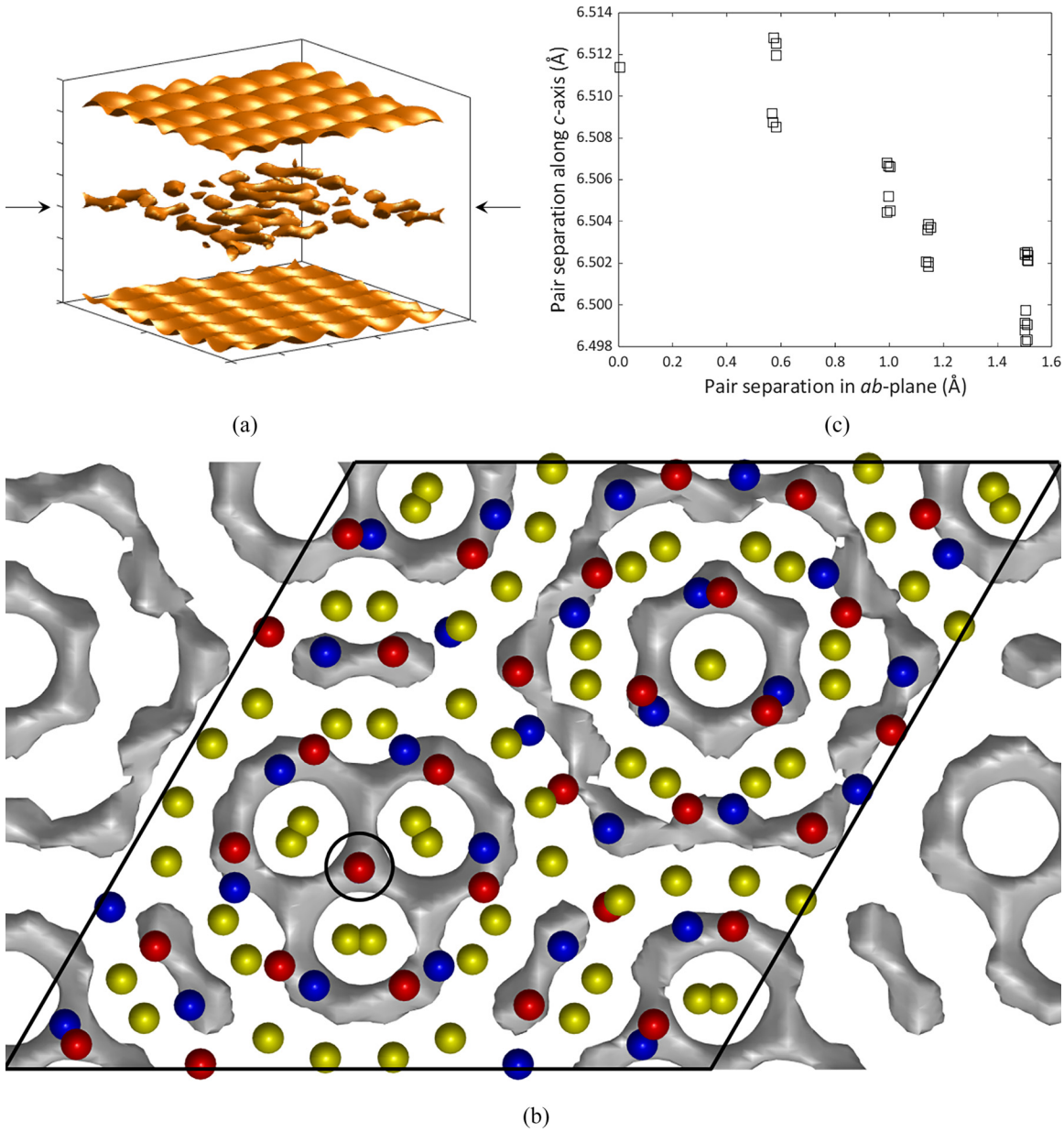

FIG. 6. (a) Electron density isosurface plot showing charge buildup, indicated by arrows, in interlayer region of a 18° twisted WS_2 bilayer. Electron density is equal to $0.000\,35\rho_{max}$, where ρ_{max} is the maximum electron density. (b) Projected image of the interlayer charge (shaded gray) as viewed along the c axis of the bilayer. Top and bottom-layer W atoms are colored red and blue, respectively, while the yellow spheres are S atoms. Circled region shows a pair of W atoms with perfect vertical registry. Parallelogram is an approximate outline of the supercell. (c) Correlation of pair spacing in the ab plane and along the c axis for nearest-neighbor W atoms (see text for further details).

WS_2 sheets in a bilayer. In the extreme case of no coupling, the bilayer is effectively two freestanding monolayers, and the normalized $J(p_z)$ profile is identical to a monolayer. Hence, any contamination present in the interlayer region would tend to decrease the fractional $\Delta J(p_z)$ values. Our DFT simulations, however, assumed that the interlayer region was contamination-free, thereby giving fractional $\Delta J(p_z)$ values larger than experiment.

IV. CONCLUSIONS

Electron Compton scattering in the TEM is used to analyze interlayer coupling in single flakes of WS_2, with the advantage of TEM over other techniques being its high spatial resolution and scattering cross section, as well as accessibility of complementary structural and chemical information about the sample. Compton $J(p_z)$ data indicated that compared to a monolayer, the electrons were more localized in a 18° twisted bilayer. Further DFT analysis showed that the localization was due to charge buildup in the interlayer region, in particular at high-energy sites consisting of vertically overlapping tungsten atoms. The excess energy of these "wrong bonds" is reduced by the charge screening, as well as a local dilation of the interlayer spacing. The optical, vibrational, and electrical properties of TMD bilayers are known to be sensitive to the twist angle. Our work uncovers the detailed nature of the

interlayer coupling mechanism, and is a valuable benchmark for further studies on other TMD systems.

Raw data for this work are published in the Durham University research data repository [51].

ACKNOWLEDGMENTS

A.T. acknowledges the UK Engineering and Physical Sciences Research Council (EPSRC) for Ph.D. funding (Grant No. EP/R513039/1) and the Japan Society for the Promotion of Science (JSPS) for support of a pre/postdoctoral research fellowship (Grant No. PE21763) in Japan. A.C., P.K.M., and A.I. gratefully acknowledge the very generous support of the Israel Science Foundation, Project No. 2596/21. Y.X. and T.M. acknowledge the Japan Ministry of Education, Culture, Sports, Science and Technology (MEXT) for funding (Grants No. 19H00818 and No. 19H05787). S.J.C. is grateful to Durham University for use of its supercomputing facilities (Hamilton), and also EPSRC under Grant No. EP/X035891/1 for the UK national supercomputing facility Archer 2.

[1] K. S. Novoselov, A. K. Geim, S. V. Morozov, D. Jiang, Y. Zhang, S. V. Dubonos, I. V. Grigorieva, and A. A. Firsov, Electric field effect in atomically thin carbon films, Science **306**, 666 (2004).

[2] A. K. Geim and K. S. Novoselov, The rise of graphene, Nat. Mater. **6**, 183 (2007).

[3] H. Liu, A. T. Neal, Z. Zhu, Z. Luo, X. Xu, D. Tománek, and D. Y. Peide, Phosphorene: An unexplored 2D semiconductor with a high hole mobility, ACS Nano **8**, 4033 (2014).

[4] P. Vogt, P. De Padova, C. Quaresima, J. Avila, E. Frantzeskakis, M. C. Asensio, A. Resta, B. Ealet, and G. Le Lay, Silicene: Compelling Experimental Evidence for Graphene-like Two-Dimensional Silicon, Phys. Rev. Lett. **108**, 155501 (2012).

[5] M. Chhowalla, H. S. Shin, G. Eda, L-J. Li, K. P. Loh, and H. Zhang, The chemistry of two-dimensional layered transition metal dichalcogenide nanosheets, Nat. Chem. **5**, 263 (2013).

[6] A. Chaves, J. G. Azadani, H. Alsalman, D. R. da Costa, R. Frisenda, A. J. Chaves, S. H. Song, Y. D. Kim, D. He, J. Zhou, A. Castellanos-Gomes, F. M. Peeters, Z. Liu, C. L. Hinkle, S-H. Oh, P. D. Ye, S. J. Koester, Y. H. Lee, Ph. Avouris, X. Wang, and T. Low, Bandgap engineering of two-dimensional semiconductor materials, npj 2D Mater. Appl. **4**, 29 (2020).

[7] B. Anasori, M. R. Lukatskaya, and Y. Gogotsi, 2D metal carbides and nitrides (MXenes) for energy storage, Nat. Rev. Mater. **2**, 16098 (2017).

[8] N. Zhang, T. Wang, X. Wu, C. Jiang, T. Zhang, B. Jin, H. Ji, W. Bai, and R. Bai, From 1D polymers to 2D polymers: Preparation of free-standing single-monomer-thick two-dimensional conjugated polymers in water, ACS Nano **11**, 7223 (2017).

[9] B. Huang, G. Clark, E. Navarro-Moratalla, D. R. Klein, R. Cheng, K. L. Seyler, D. Zhong, E. Schmidgall, M. A. McGuire, D. H. Cobden, W. Yao, D. Xiao, P. Jarillo-Herrero, and X. Xu, Layer-dependent ferromagnetism in a van der Waals crystal down to the monolayer limit, Nature (London) **546**, 270 (2017).

[10] Z. Fei, T. Palomaki, S. Wu, W. Zhao, X. Cai, B. Sun, P. Nguyen, J. Finney, X. Xu, and D. H. Cobden, Edge conduction in monolayer WTe_2, Nat. Phys. **13**, 677 (2017).

[11] X. Xi, Z. Wang, W. Zhao, J-H. Park, K. T. Law, H. Berger, L. Forró, J. Shan, and K. F. Mak, Ising pairing in superconducting $NbSe_2$ atomic layers, Nat. Phys. **12**, 139 (2016).

[12] K. F. Mak, C. Lee, J. Hone, J. Shan, and T. F. Heinz, Atomically Thin MoS_2: A New Direct-Gap Semiconductor, Phys. Rev. Lett. **105**, 136805 (2010).

[13] K. S. Novoselov, A. Mishchenko, A. Carvalho, and A. H. Castro Neto, 2D materials and van der Waals heterostructures, Science **353**, aac9439 (2016).

[14] Y. Cao, V. Fatemi, S. Fang, K. Watanabe, T. Taniguchi, E. Kaxiras, and P. Jarillo-Herrero, Unconventional superconductivity in magic-angle graphene superlattices, Nature (London) **556**, 43 (2018).

[15] Y. Cao, V. Fatemi, A. Demir, S. Fang, S. L. Tomarken, J. Y. Luo, J. D. Sanchez-Yamagishi, K. Watanabe, T. Taniguchi, E. Kaxiras, R. C. Ashoori, and P. Jarillo-Herrero, Correlated insulator behavior at half-filling in magic-angle graphene superlattices, Nature (London) **556**, 80 (2018).

[16] K. Tran, G. Moody, F. Wu, X. Lu, J. Choi, K. Kim, A. Rai, D. A. Sanchez, J. Quan, A. Singh, J. Embley, A. Zepeda, M. Campbell, T. Autry, T. Taniguchi, K. Watanabe, N. Lu, S. K. Banerjee, K. L. Silverman, S. Kim, E. Tututc, L. Yang, A. H. MacDonald, and X. Li, Evidence of moiré excitons in van der Waals heterostructures, Nature (London) **567**, 71 (2019).

[17] Q. H. Wang, K. Kalantar-Zadeh, A. Kis, J. N. Coleman, and M. S. Strano, Electronics and optoelectronics of two-dimensional transition metal dichalcogenides, Nat. Nanotechnol. **7**, 699 (2012).

[18] F. Xia, H. Wang, D. Xiao, M. Dubey, and A. Ramasubramaniam, Two-dimensional material nanophotonics, Nat. Photonics **8**, 899 (2014).

[19] S-K. Mo, Angle-resolved photoemission spectroscopy for the study of two-dimensional materials, Nano Convergence **4**, 6 (2017).

[20] W. Jin, P-C. Yeh, N. Zaki, D. Zhang, J. T. Sadowski, A. Al-Mahboob, A. M. van der Zande, D. A. Chenet, J. I. Dadap, I. P. Herman, P. Sutter, J. Hone, and R. M. Osgood, Direct Measurement of the Thickness-Dependent Electronic Band Structure of MoS_2 Using Angle-Resolved Photoemission Spectroscopy, Phys. Rev. Lett. **111**, 106801 (2013).

[21] M. Dendzik, M. Michiardi, C. Sanders, M. Bianchi, J. A. Miwa, S. S. Grønborg, J. V. Lauritsen, A. Bruix, B. Hammer, and P. Hofmann, Growth and electronic structure of epitaxial single-layer WS_2 on Au (111), Phys. Rev. B **92**, 245442 (2015).

[22] H. M. Hill, A. F. Rigosi, K. T. Rim, G. W. Flynn, and T. F. Heinz, Band alignment in MoS_2/WS_2 Transition metal dichalcogenide heterostructures probed by scanning tunneling microscopy and spectroscopy, Nano Lett. **16**, 4831 (2016).

[23] M.-K. Lin, G.-H. Chen, C.-L. Ho, W.-C. Chueh, J. A. Hlevyack, C.-N. Kuo, T.-Y. Fu, J.-J. Lin, C. S. Lue, W.-H. Chang, N. Takagi, R. Arafune, T.-C. Chiang, and C.-L. Lin, Tip-mediated

bandgap tuning for monolayer transition metal dichalcogenides, ACS Nano **16**, 14918 (2016).

[24] R. M. Feenstra, G. R. Frazier, Y. Pan, S. Fölsch, Y.-C. Lin, B. Jariwala, K. Zhang, and J. A. Robinson, Acquisition and analysis of scanning tunnelling spectroscopy data-WSe_2 monolayer, J. Vac. Sci. Technol., A **39**, 011001 (2021).

[25] S. W. Jung, S. Pak, S. Lee, S. Reimers, S. Mukherjee, P. Dudin, T. K. Kim, M. Cattelan, N. Fox, S. S. Dhesi, C. Cacho, and S. N. Cha, Spectral functions of CVD grown MoS_2 monolayers after chemical transfer onto Au surface, Appl. Surf. Sci. **532**, 147390 (2020).

[26] B. G. Williams, T. G. Sparrow, and R. F. Egerton, Electron Compton scattering from solids, Proc. R. Soc. London, Ser. A **393**, 409 (1984).

[27] Z. Feng, X. Zhang, Y. Sakurai, Z. Wang, H. Li, and H. Hu, Compton profile of few-layer graphene investigated by electron energy-loss spectroscopy, Sci. Rep. **9**, 17313 (2019).

[28] M. J. Cooper, Compton scattering and electron momentum determination, Rep. Prog. Phys. **48**, 415 (1985).

[29] M. R. Molas, K. Nogajewski, A. O. Slobodeniuk, J. Binder, M. Bartos, and M. Potemski, The optical response of monolayer, few-layer and bulk tungsten disulfide, Nanoscale **9**, 13128 (2017).

[30] W. Zhao, Z. Ghorannevis, L. Chu, M. Toh, C. Kloc, P-H. Tan, and G. Eda, Evolution of electronic structure in atomically thin sheets of WS_2 and WSe_2, ACS Nano **7**, 791 (2013).

[31] M. Liao, Z. Wei, L. Du, Q. Wang, J. Tang, H. Yu, F. Wu, J. Zhao, X. Xu, B. Han, K. Liu, P. Gao, T. Polcar, Z. Sun, D. Shi, R. Yang, and G. Zhang, Precise control of the interlayer twist angle in large scale MoS_2 homostructures, Nat. Commun. **11**, 2153 (2020).

[32] A. Cohen, A. Patsha, P. K. Mohapatra, M. Kazes, K. Ranganathan, L. Houben, D. Oron, and A. Ismach, Growth-etch metal-organic chemical vapor deposition approach of WS_2 atomic layers, ACS Nano **15**, 526 (2021).

[33] A. Cohen, P. K. Mohapatra, S. Hettler, A. Patsha, K. V. L. V. Narayanachari, P. Shekhter, J. Cavin, J. M. Rondinelli, M. Bedzyk, D. Oswaldo, R. Arenal, and A. Ismach, Tungsten oxide mediated quasi-van der Waals epitaxy of WS_2 on sapphire, ACS Nano **17**, 5399 (2023).

[34] A. Gurarslan, Y. Yu, L. Su, Y. Yu, F. Suarez, S. Yao, T. Zhu, M. Ozturk, Y. Zhang, and L. Cao, Surface-energy-assisted perfect transfer of centimeter-scale monolayer and few layer MoS_2 films onto arbitrary substrates, ACS Nano **8**, 11522 (2014).

[35] A. Talmantaite, M. R. C. Hunt, and B. G. Mendis, Electron Compton scattering and the measurement of electron momentum distributions in solids, J. Microsc. **279**, 185 (2020).

[36] S. J. Clark, M. D. Segall, C. J. Pickard, P. J. Hasnip, M. I. J. Probert, K. Refson, and M. C. Payne, First principles methods using CASTEP, Z. Kristallogr. **220**, 567 (2005).

[37] A. P. Bartók and J. R. Yates, Regularized SCAN functional, J. Chem. Phys. **150**, 161101 (2019).

[38] J. Singleton, *Band Theory and Electronic Properties of Solids* (Oxford University Press, Oxford, 2012).

[39] X. Zhao, J. Kotakoski, J. C. Meyer, E. Sutter, P. Sutter, A. V. Krasheninnikov, U. Kaiser, and W. Zhou, Engineering and modifying two-dimensional materials by electron beams, MRS Bull. **42**, 667 (2017).

[40] See Supplemental Material at http://link.aps.org/supplemental/10.1103/PhysRevB.107.235424 containing (i) SAED analysis of electron-beam damage in monolayer WS_2; (ii) Electron binding energy and Compton scattering; (iii) $J(p_z)$ profiles for monolayer WS_2; (iv) Bilayer SAED patterns and Compton scattering vectors; (v) Coincident site lattice for 18 ° twist-angle WS_2 bilayer; (vi) CASTEP simulated $J(p_z)$ profiles; and (vii) Electron density isosurfaces for *AB* stacked WS_2 bilayer.

[41] A. Savitzky and M. J. E. Golay, Smoothing and differentiation of data by simplified least squares procedures, Anal. Chem. **36**, 1627 (1964).

[42] H. Zeng, G. B. Liu, J. Dai, Y. Yan, B. Zhu, R. He, L. Xie, S. Xu, X. Chen, W. Yao, and X. Cui, Optical signature of symmetry variations and spin-valley coupling in atomically thin tungsten dichalcogenides, Sci. Rep. **3**, 1608 (2013).

[43] T. A. Carlson, *Photoelectron and Auger Spectroscopy* (Plenum Press, New York, 1975).

[44] B. G. Mendis and A. Talmantaite, Towards electron energy loss Compton spectra free from dynamical diffraction artefacts, Microsc. Microanal. **28**, 1971 (2022).

[45] Y. Xie, K. Shibata, and T. Mizoguchi, Interface_master: Python package building CSL and approximate CSL interfaces of any two lattices- an effective tool for interface engineers, arXiv:2211.15173.

[46] H. Yoo, R. Engelke, S. Carr, S. Fang, K. Zhang, P. Cazeaux, S. H. Sung, R. Hovden, A. W. Tsen, T. Taniguchi, K. Watanabe, G.-C. Yi, M. Kim, M. Luskin, E. B. Tadmor, E. Kaxiras, and P. Kim, Atomic and electronic reconstruction at the van der Waals interface in twisted bilayer graphene, Nat. Mater. **18**, 448 (2019).

[47] M. R. Rosenberger, H.-J. Chuang, M. Phillips, V. P. Oleshko, K. M. McCreary, S. V. Sivaram, S. C. Hellberg, and B. T. Jonker, Twist angle-dependent atomic reconstruction and moiré patterns in transition metal dichalcogenides heterostructures, ACS Nano **14**, 4550 (2020).

[48] Z. Hennighausen, C. Lane, I. G. Buda, V. K. Mathur, A. Bansil, and S. Kar, Evidence of a purely electronic two-dimensional lattice at the interface of TMD/Bi_2Se_3 heterostructures, Nanoscale **11**, 15929 (2019).

[49] K. Liu, L. Zhang, T. Cao, C. Jin, D. Qiu, Q. Zhou, A. Zettl, P. Yang, S. G. Louie, and F. Wang, Evolution of interlayer coupling in twisted molybdenum disulfide bilayers, Nat. Commun. **5**, 4966 (2014).

[50] P.-C. Yeh, W. Jin, N. Zaki, J. Kunstmann, D. Chenet, G. Arefe, J. T. Sadowsky, J. I. Dadap, P. Sutter, J. Hone, and R. M. Osgood, Direct measurement of the tunable electronic structure of bilayer MoS_2 by interlayer twist, Nano Lett. **16**, 953 (2016).

[51] http://doi.org/10.15128/r1vx021f16r.